



HAL
open science

Wave propagation through an elastically asymmetric architected material

Vladislav A Yastrebov

► **To cite this version:**

Vladislav A Yastrebov. Wave propagation through an elastically asymmetric architected material. *Comptes Rendus. Mécanique*, 2022, <10.5802/crmeca.100>. <hal-03874750>

HAL Id: hal-03874750

<https://hal.science/hal-03874750v1>

Submitted on 28 Nov 2022

HAL is a multi-disciplinary open access archive for the deposit and dissemination of scientific research documents, whether they are published or not. The documents may come from teaching and research institutions in France or abroad, or from public or private research centers.

L'archive ouverte pluridisciplinaire **HAL**, est destinée au dépôt et à la diffusion de documents scientifiques de niveau recherche, publiés ou non, émanant des établissements d'enseignement et de recherche français ou étrangers, des laboratoires publics ou privés.



HAL Authorization



INSTITUT DE FRANCE
Académie des sciences

Comptes Rendus

Mécanique


Vladislav A. Yastrebov

Wave propagation through an elastically asymmetric architected material

Volume 350 (2022), p. 1-26

<<https://doi.org/10.5802/crmeca.100>>

© Académie des sciences, Paris and the authors, 2022.
Some rights reserved.

 This article is licensed under the
CREATIVE COMMONS ATTRIBUTION 4.0 INTERNATIONAL LICENSE.
<http://creativecommons.org/licenses/by/4.0/>



*Les Comptes Rendus. Mécanique sont membres du
Centre Mersenne pour l'édition scientifique ouverte*
www.centre-mersenne.org



Short paper / Note

Wave propagation through an elastically asymmetric architected material

La propagation des ondes à travers des milieux élastiquement asymétriques

Vladislav A. Yastrebov^{Ⓢ a}

^a MINES ParisTech, PSL University, Centre des Matériaux, CNRS UMR 7633, BP 87, 91003, Evry, France

E-mail: vladislav.yastrebov@mines-paristech.fr

Abstract. A one-dimensional wave propagation through elastically asymmetric media is investigated. A class of metamaterials possessing an arbitrary elastic asymmetry is proposed. This asymmetry results in different wave speeds of tensile and compressive components of elastic waves. The faster component can overtake the slower one resulting in their dissipative annihilation through energy cascades. Efficient absorbing assemblies are presented and analysed numerically. The length of the asymmetric part needed to damp a harmonic signal is determined analytically and validated numerically. Transmission properties for random self-affine wave packets are studied: a universal scaling for the transmission factor variation with the length of the asymmetric part was established.

Résumé. La propagation unidimensionnelle des ondes à travers des milieux élastiquement asymétriques est étudiée. Une classe de métamatériaux possédant une asymétrie élastique arbitraire est proposée. Cette asymétrie entraîne différentes vitesses des composants de traction et de compression : le composant le plus rapide dépasse le plus lent, entraînant leur annihilation dissipative par des cascades d'énergie. Des assemblages de damping efficace sont présentés et analysés numériquement. La longueur de la partie asymétrique nécessaire pour amortir un signal harmonique est déterminée analytiquement et validée numériquement. Les propriétés de transmission pour les paquets d'ondes auto-affines aléatoires sont étudiées : une mise à l'échelle universelle pour la variation du facteur de transmission avec la longueur de la partie asymétrique a été établie.

Keywords. Elastic asymmetry, Wave damping, Wave propagation, Wave annihilation, Architected material, Internal contact.

Mots-clés. Asymétrie élastique, Damping des ondes, Propagation des ondes, Annihilation des ondes, Matériaux architecturés, Contacts internes.

2020 Mathematics Subject Classification. 74J30.

Manuscript received 25th January 2021, revised 4th September 2021, accepted 30th November 2021.

1. Introduction

Elastically asymmetric materials are rather common in nature and include granular materials, soils, materials with internal flaws (e.g. cracked rocks, concrete) and others [1]. Natural materials are in general stiffer in compression than in tension due to respective closing and opening of internal cracks [2]. However, there is a class of structures and materials which have the opposite asymmetry, i.e. they can be hard-in-tension and soft-in-compression, like wires/ropes and fibre networks, whose elements buckle under compressive loads [3–5]. In soft matter, living cells, due to elastic asymmetry of fibrin and collagen, are able to self-adjust in response to external loads [6–10]. However, for most *solid* materials the elastic asymmetry is rather small, it could be also centred not at zero deformation, and is hard to control. In contrast, the asymmetry could be infinitely high in granular chains or granular crystals, which represent a particular class of artificial assemblies whose asymmetry and non-linearity comes from the contact interaction [11–13]. In addition to elastic or inelastic asymmetry [14, 15], the asymmetry of the interfacial behaviour is relevant for many systems: for example, the asymmetry of the skin drag in marine fauna [16] or asymmetry of friction in natural (e.g., fur, snake skin) or artificial (e.g., ski-tour skis, kirigami) systems [17, 18]. Finally, a particular type of asymmetry, which is non-centred at zero, exists in mechanical response of rate-independent elasto-plastic materials at the yield surface, and also in materials experiencing twinning [14], however, these types of *inelastic* asymmetry are out of scope of the present discussion.

Mechanical behaviour of elastically asymmetric materials depends on the “directionality” of the strain tensor, i.e. on the signs of principal strains. Here, we define an elastically asymmetric material as a material for which exist such orientations of the strain tensor $\bar{\boldsymbol{\varepsilon}}$ that the following statement holds

$$\forall \delta \ll 1: \boldsymbol{\sigma}(\delta \bar{\boldsymbol{\varepsilon}}) \neq -\boldsymbol{\sigma}(-\delta \bar{\boldsymbol{\varepsilon}}), \quad (1)$$

where $\boldsymbol{\sigma}$ is the Cauchy stress tensor, δ is the amplitude factor, and $\delta \bar{\boldsymbol{\varepsilon}}$ is the infinitesimal strain tensor. Materials with such asymmetry are called heteromodular, bimodulus or bimodular. Therefore, the Young’s shear and bulk moduli of such materials depend on the loading direction and on its sign. Obviously, because of this asymmetry only “one-sided” derivatives or directional derivatives for the elastic tensor can be defined:

$$\mathbf{C}(\bar{\boldsymbol{\varepsilon}}) = \left. \frac{\partial \boldsymbol{\sigma}}{\partial \boldsymbol{\varepsilon}} \right|_{\text{dir}=\bar{\boldsymbol{\varepsilon}}}.$$

These elastically asymmetric materials, while retaining their strong asymmetry, can remain linear in the sense of argument multiplication (amplitude independent):

$$\boldsymbol{\sigma}(\alpha \boldsymbol{\varepsilon}) = \alpha \boldsymbol{\sigma}(\boldsymbol{\varepsilon}), \quad \forall \alpha \geq 0, \quad (2)$$

but not in the sense of superposition

$$\boldsymbol{\sigma}(\boldsymbol{\varepsilon}_1 + \boldsymbol{\varepsilon}_2) \neq \boldsymbol{\sigma}(\boldsymbol{\varepsilon}_1) + \boldsymbol{\sigma}(\boldsymbol{\varepsilon}_2).$$

In addition to this asymmetry, elastic anisotropy often comes into play [19, 20]. For elastically asymmetric and isotropic materials, in particular case, the relation between the stresses and strains can be formulated in terms of principal values [1, 21], with the anisotropic and asymmetric materials, the situation is more complicated: for example, a formulation of constitutive relations for orthotropic materials can be found in [22, 23]. However, to the best of the author’s knowledge, a general theory of elastic anisotropic asymmetry in which the anisotropy comes from a particular asymmetry direction, which could be further combined with the independent anisotropy of the

material itself, does not exist. A more general class of materials, for which, at given configuration $\{\boldsymbol{\varepsilon}_0, \boldsymbol{\sigma}\}$, the following statement holds:

$$-\boldsymbol{\sigma}(\boldsymbol{\varepsilon}_0 - \delta\bar{\boldsymbol{\varepsilon}}) \neq \boldsymbol{\sigma}(\boldsymbol{\varepsilon}_0 + \delta\bar{\boldsymbol{\varepsilon}}), \quad \text{for } \|\delta\bar{\boldsymbol{\varepsilon}}\| \rightarrow 0,$$

cannot be called elastically asymmetric. Since such materials for $\forall \boldsymbol{\varepsilon}_0 \neq 0$ do not demonstrate asymmetric behaviour centred at zero strain, the linearity in the sense of (2) is lost. Since this property is an essential feature for the following analysis, this class of materials is out of scope of the current study.

The general theory of heteromodular materials was developed by Ambartsumyan in a series of pioneering papers [21, 24] and others, which were later summarized in a monograph [25], which apart from the general formulation contains plenty of solutions for mechanical problems. Among additional solutions obtained by other authors and presenting a fundamental interest is the solution of Boussinesq problem obtained in [26], which, however, cannot be readily used within the superposition principle because of the inherent non-linearity. Different attempts to extend the theory of heteromodulus materials exist, using different combinations of invariants [25, and references therein], e.g. using the first stress invariant and the second deviatoric invariant [27] or all three of them [28, 29]. A slightly more general non-linear theory for heteromodulus materials was given in [30] by Green and Mkrtychian, one of the followers of Ambratsumyan. In [28] a link between wave propagation velocities and elastic properties within a rather general model based on all three strain invariants was derived and used for few data provided in [25]. Other theoretical results on the statics of asymmetric materials could be found in [1, 31–33].

However, the most interesting and intriguing effects these materials demonstrate is in dynamics. Because of the strong and amplitude-independent non-linearity, these materials obey strongly unconventional wave propagation and vibrational patterns. Nevertheless, such behaviour has not yet been fully investigated: the propagation of elastic waves in asymmetric media was studied in [34–38]. Since the propagation of compressive and tensile parts follow a simple linear non-dispersive equation, the particularity of such studies reduces to the understanding of propagation of particular points such as signotons, semi-signotons and shocks, the points at which the deformation changes its sign, and their motion, emergence and annihilation follow very non-trivial behaviour [34]. Several simple scenarios of one-dimensional wave propagation in heterogeneous medium were treated analytically in [39]¹ and numerically in [40]. The problem of one-dimensional wave propagation in elastically asymmetric medium was studied from the non-reciprocity point of view in [41]; studies on non-reciprocity of wave motion in other types of systems could be found in works of Vakakis and collaborators [42, e.g.] among many others. In general, the non-reciprocity provides a powerful control over the wave propagation, which could be used to construct, for example, acoustic diodes [43] and other exotic devices. In [41] a spatial modulation of the elastic asymmetry was investigated following a very similar set-up to the one considered in the current paper; by combining spatial modulation the authors obtained a controllable non-reciprocity for a simple incident signal containing a single tensile and compressive components. This study was followed by a detailed investigation of non-reciprocity in a single asymmetric spring element in the interface between symmetric media carried out by the same authors [44]. The theory of Green and Mkrtychian [30], adjusted for the case of isotropic heterogeneous material in infinitesimal deformations, was used by Benveniste in [45] to obtain solutions for plane and spherical waves for compressible and incompressible heteromodulus materials, which demonstrated a peculiar (for the classical elasticity) propagation of a coupled longitudinal and shear wave at the same speed.

¹The reader has to use caution in handling the first presented example considered in this paper: the amplitude of the shock wave increases gradually starting from zero amplitude, which is not explicitly showed in the paper.

In terms of spatio-temporal numerical integration of wave equations in an asymmetric medium, shock waves naturally formed because of the overlap of tensile and compressive waves result in emergence of spurious oscillations. To handle better this artefact, an adapted integration technique could be used. In [46] the authors suggested a collocation and least-squares (CLS) method, which over-performs other alternative integration methods in terms of accuracy and in simplicity of use. It is worth mentioning here that such a strongly non-linear hyperbolic problem with inherent shock waves and other discontinuities has to be treated using general energetic principles and so-called entropy conditions formulated in [47], notably the choice between possible solution has to follow the principle of the growth of entropy of particles crossing the shock front. Application of these principles to selection of physical solutions in bi-linear (a generalization of the elastic asymmetry) [48–51] and also tri-linear systems was carried out in [50]. Interestingly, the latter case, also relevant for contact-based metamaterials, apart from entropy inequality requires additional conditions on isolation of physically feasible solutions.

Vibration of heteromodal was studied by many authors, whose contributions are well summarized in [52], where some fundamental results were obtained for gyroscopic and non-gyroscopic systems using analytical and numerical tools. The approaches used in the above-cited paper were developed in earlier works on vibration of systems with internal impacts, which render them elastically asymmetric, among them we could cite [53–55], more results are summarized in the monograph [56].

Here, we focus on a particular property of the overlap of compressive and tensile components, which could result in a very efficient annihilation of the waves if some damping is present in the system. This phenomenon was already studied theoretically and numerically in [36, 37], here we carry out a numerical analysis with a different perspective for simple and, more complex, realistic incident wave patterns and obtain a more general conclusion for the energy damping as well as for signal deformation and polarization.

The structure of the paper is as follows, we present a new class of materials with controllable and arbitrary asymmetry centred at zero, this asymmetry comes from internally architected contacts (Section 2). After presenting the governing equations and the solution methods in Sections 3, 4, to start, we show simple simulations of a mono-harmonic elastic wave propagating in bimodal one-dimensional medium (Section 5). The damping properties of simple assemblies of bimodal materials are studied in Sections 6, 7. A more general study of the damping properties for random nominally self-affine and compact incident wave packets is conducted in Section 8, in Section 9 we develop a simple geometrical model to explain the observed behaviour. We conclude in Section 10.

2. Architected materials with internal contacts

First, we propose a class of architected materials with an elastic asymmetry, which emerges from internal contacts between parts of the elemental cell (see Figure 1). This asymmetry is controllable and reversible, non-destructive and arbitrary-strong, contrary to a marginal asymmetry occurring in natural solid materials. The idea behind this novel architecture is that the non-adhesive contact can bear only compressive loads and opens in case of tensile ones. This non-smooth and amplitude-independent non-linearity renders the internal contact a good candidate for widening or enhancing novel and meta properties of architected materials (see e.g. [57–59]). For example, if a zero-thickness cut is introduced in the material, as shown in Figure 1(a), the resulting elastic modulus along, for example, OY direction depends on the sign of the applied deformation: in case of tension, only thin ligaments bear the load and thus macroscopically the material behaves as a soft one; on the contrary, in compression, the contact in the cut is closed and can

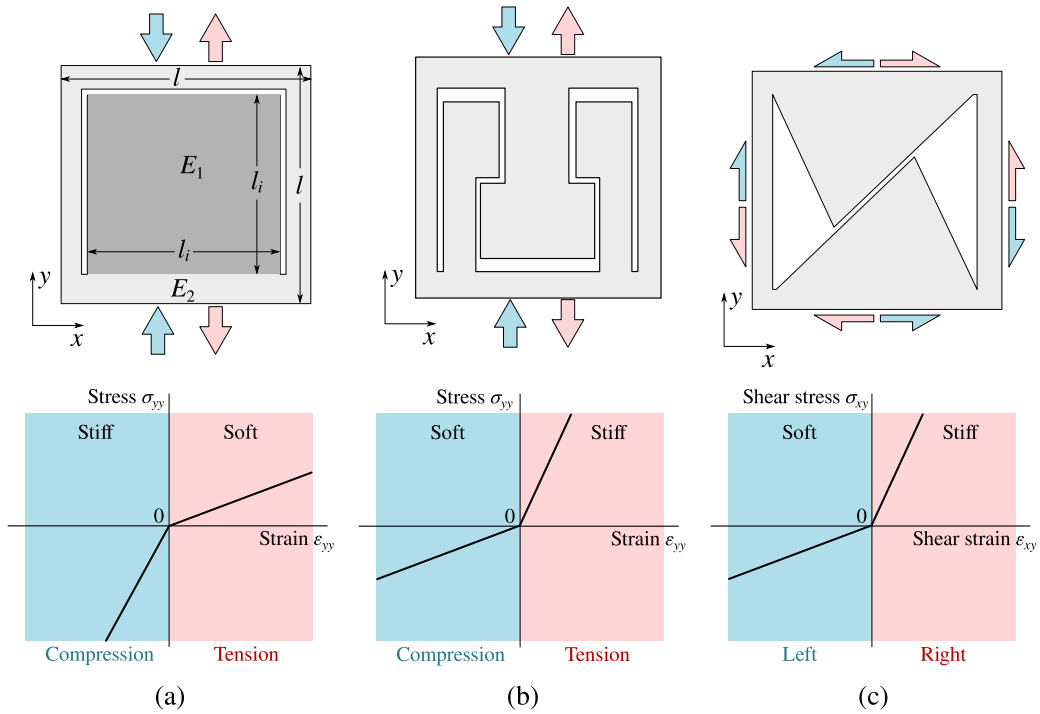


Figure 1. Examples of design of elemental architected cells with asymmetric elastic properties: the effective stiffness depends on the sign of the axial strain component (compression/tension): architecture (a) is soft-in-tension and stiff-in-compression; architecture (b) is stiff-in-tension and soft-in-compression (within a certain limit); architecture (c) is shear-asymmetric. The associated deformation curves are also shown.

fully bear the load, thus resulting in a stiffer elastic behaviour. The elastic asymmetry can be controlled by the dimensions of the cut and by materials used in the central and peripheral zones. For the simple heterogeneous design presented in Figure 1(a), a rough estimation of the ratio of the Young’s moduli in tension E^+ and compression E^- can be given from simple geometrical consideration as

$$\frac{E^+}{E^-} \approx \left(1 - \frac{l_i}{l}\right) \frac{E_2}{E_1},$$

where l is the square-cell size, l_i is the side-length of Π -shape cut, and $E_{1,2}$ are Young’s moduli of the inner and outer materials: to amplify the asymmetry, materials can be chosen such that $E_1 > E_2$. Thus, the resulting asymmetry can greatly overpass the asymmetry of existing materials, which are stiffer in compression than in tension, such as rocks and concrete. The opposite asymmetry also occurs in Nature in fibrous materials [5, 60–62] and living cells [8]: this asymmetry is based on local buckling of fibres under compression. In contrast to this mechanism, our architecture uses contact interaction to achieve comparable asymmetry. A novel stiff-in-tension and soft-in-compression architecture is presented in Figure 1(b): the contact is activated in tension and renders the material stiffer than in compression; in the latter case only thin ligaments bear the load as far as the gap remains open. The asymmetry of this material can be also enhanced by combination of stiff and soft materials in the architecture. The shear-enhanced asymmetry can be obtained, for example, through the design presented in Figure 1(c).

Such materials demonstrate unusual properties in dynamics both in vibration and wave propagation [37, 54, 63]. The latter presents the main topic of this paper. Namely, we study propagation of elastic waves through a one-dimensional assembly of symmetric and asymmetric materials, the focus is put on the damping properties and further on the signal form change. We show that the elastic asymmetry modifies the energy dissipation mechanisms, ensuring rapid damping even for low-frequency signals.

3. Wave equation

A one-dimensional wave equation for longitudinal waves propagating through a bimodular elastic material [34] with viscous dissipation of Kelvin–Voigt type (an elastic spring connected in parallel with a damper) [64] is of the form:

$$u_{,tt} = \frac{E}{\rho}(u_{,x} + \alpha|u_{,x}|)_{,x} + \frac{\mu}{\rho}u_{,xxt}, \quad -1 < \alpha < 1, \quad (3)$$

where u is the axial displacement, lower indices after comma denote partial derivation $\bullet_{,x}$ and $\bullet_{,t}$ with respect to coordinate and time, respectively; ρ is the mass density (kg/m^3), E is the elastic modulus (Pa), and μ is the viscosity (Pa·s). The dimensionless factor α determines the material asymmetry: the elastic moduli are equal to

$$E^+ = E(1 + \alpha), \quad E^- = E(1 - \alpha)$$

in tension ($u_{,x} > 0$) and compression ($u_{,x} < 0$), respectively. Thus, the tensile and compressive components of elastic waves propagate at different speeds given by

$$c^\pm = \sqrt{E^\pm / \rho}.$$

Note that for a signal which has either purely compressive or tensile deformation, the wave propagation is governed by a linear Kelvin–Voigt model, however the superposition principle for deformation of different signs does not hold. The behaviour is independent of the signal amplitude since the non-linearity is localized in a single point on deformation curve (change of sign), which is centred at zero deformation. For one-dimensional systems, *elastic asymmetry* reduces to *bimodular* material model, thus hereinafter these two terms will be used interchangeably.

4. Methods

We first consider propagation of elastic waves in structures made of materials shown in Figure 1(a,b); the structure includes one or two segments with bimodular materials. Oscillations are induced at an excitation point in an elastically symmetric segment of a bar by applying a harmonic force $f = f_0 \sin(\omega_0 t)$ or a more complicated force as will be discussed in Section 8. Forcing frequency ω_0 is chosen in the interval in which viscous effects are almost negligible, i.e. $\mu\omega_0 / \rho c^{\pm 2} \ll 1$. The induced elastic waves propagate to the left and to the right: on the left they are absorbed by an absorbing layer. On the right they pass through a single segment of length L of bimodular material [*Configuration 1*, see Figure 1(c)], which without loss of generality can be considered to be stiff-in-tension and soft-in-compression, i.e. $\alpha_1 > 0$ and $E_1^+ > E_1^-$. In addition, we consider *Configuration 2* (see Figure 2(b)), which has an extra segment of a bimodular material with the opposite asymmetry, i.e. it is soft-in-tension and stiff-in-compression ($\alpha_2 = -\alpha_1 < 0$, $E_2^+ < E_2^-$). The bimodular segment(s), are followed by a symmetric elastic bar with an absorbing layer on its extremity. The equations of motion are solved numerically using finite differences and Störmer–Verlet integrator. Since all the absorbing boundaries bound symmetric segments,

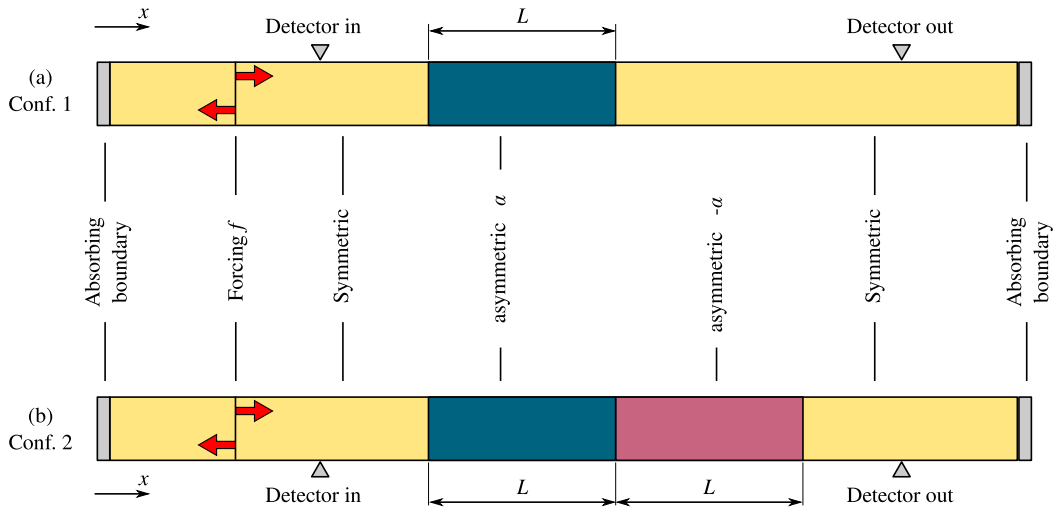


Figure 2. Configurations 1 and 2, which are used to study one-dimensional wave propagation in asymmetric media, are depicted in (a) and (b), respectively.

we enforce there $u_{,t} = \pm c_0 u_{,x}$ with the minus and plus sign at the right and left boundaries, respectively, see implementation in [65]. The spatial discretization unit l reflects the size of the architected elemental cell, thus the boundaries between symmetric and asymmetric segments pass between two springs separated by the concentrated mass. If $\lambda_0 \gg l$ (where λ_0 is a signal wavelength), such a homogenized model represents an effective medium for asymmetric architected materials with internal contacts. The model is less reliable for short wavelengths $\lambda/l \sim 1$, but can be viewed as a first-order approximation.

5. Simple examples

In this section to a large extent we follow the work of [36]. Consider Configuration 1 with a single wave

$$u_{,t}(x, t) \approx \begin{cases} -v_0 \sin\left(\omega_0 \left(\frac{x}{c_0} - t\right)\right), & \text{if } 0 \leq t - \frac{x}{c_0} \leq \frac{2\pi}{\omega_0} \\ 0, & \text{elsewhere} \end{cases}$$

propagating from the forcing point to the right ($\omega_0 > 0$) at speed c_0 in the elastically symmetric segment. To avoid high-frequency oscillations at extremities of the signal, we used a Gaussian smoothing to initiate this localized wave, i.e. the following forcing was applied

$$f = \begin{cases} \text{sign}(\omega_0)[e(t, 3) - e(t, 5)], & \text{if } 0 \leq t \leq 4\pi/|\omega_0| \\ 0, & \text{otherwise,} \end{cases}$$

where $e(t, t'_0) = \exp(-2|\omega_0|t/\pi - t'_0)^2$. In the vicinity of $t = 2\pi/\omega_0$ such forcing is very similar to $f = \sin(\omega_0 t - \pi)$, but it produces a smoother signal. In this wave propagating to the right, the tensile component is followed by a compressive one. We assume, that the elastic modulus of the symmetric segment is equal to the compressive modulus of the bimodular material $E_0 = E^-$ and $c_0 = c^-$. When this single wave enters the bimodular segment, the tensile component accelerates abruptly and propagates at speed $c^+ > c^-$, whereas the compressive component continues to propagate at the same speed c^- and passes smoothly from symmetric to bimodular segment, and further to the other symmetric segment (see Figures 3(a) and 4(a)). In contrast, the tensile component is partly reflected back towards the emitter because of the elastic contrast: it occurs

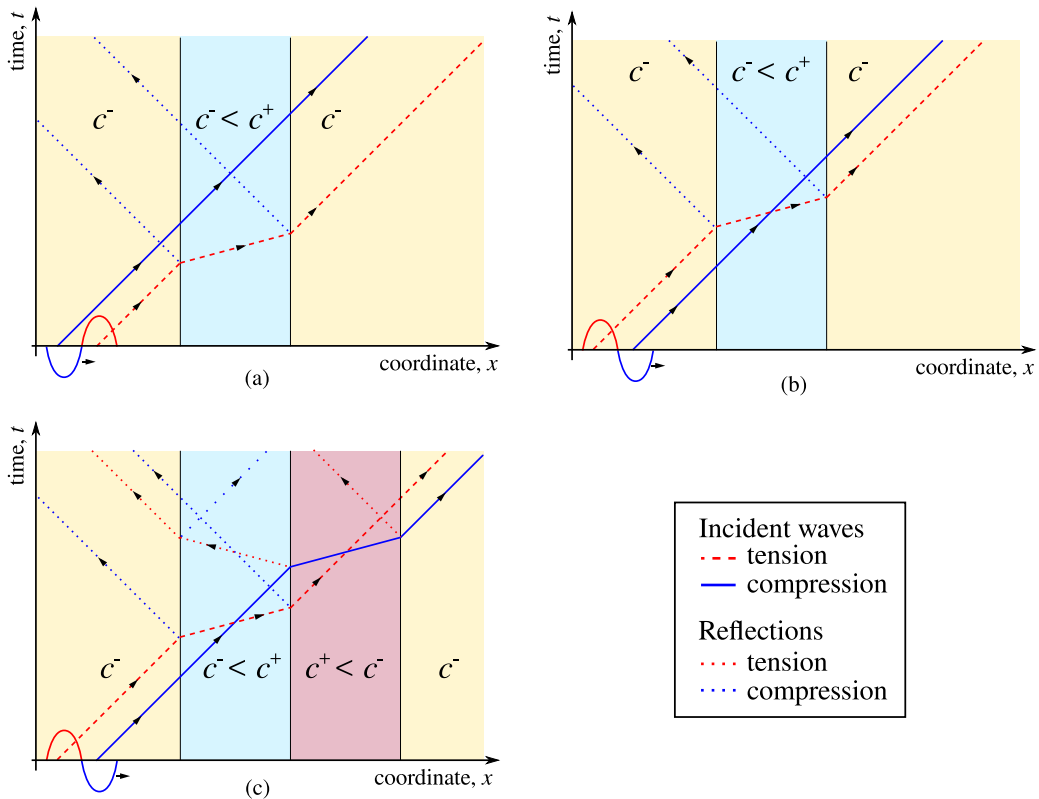


Figure 3. Spatio-temporal wave tracing is presented in (a) for a tensile component (dashed line) followed by a compressive one (solid line), (b) inverse incident signal, (c) inverse incident signal passing through a configuration with sections of opposite asymmetries; (a,b) and (c) correspond to Configurations 1 and 2, respectively (see Figure 2(a,b)).

on entering and escaping the bimodular segment. Within the bimodular segment, because of the difference in wave speed of the compressive and tensile components, on re-entering into elastically symmetric segment, these two components are separated by $\Delta t = L/(c^+ - c^-)$ in time and by $\Delta x = L/(1 - c^-/c^+)$ in space (so-called “rigid domain” following the terminology from [36]). These properties can be used to construct a wave filter, which (1) due to reflection can partly attenuate the passage of either tensile or compressive wave components, and (2) due to contrast in speeds can separate the tensile and compressive components in space/time.

If the order of wave components is reversed (Figure 3(b)), i.e. $\omega_0 < 0$, then the compressive component precedes the tensile one, and the system dynamics becomes more complex. The slow leading component is overtaken by the faster tensile one and they start to interfere. Note that contrary to the purely symmetric case considered in [37], the ratio of amplitudes of the tensile and compressive components propagating in the bimodular segment is given by

$$A^+/A^- = 2/(1 + c^+/c^-)$$

(due to the reflection at the interface symmetric/asymmetric material), and their wavelengths relate as

$$\lambda^-/\lambda^+ = c^-/c^+.$$

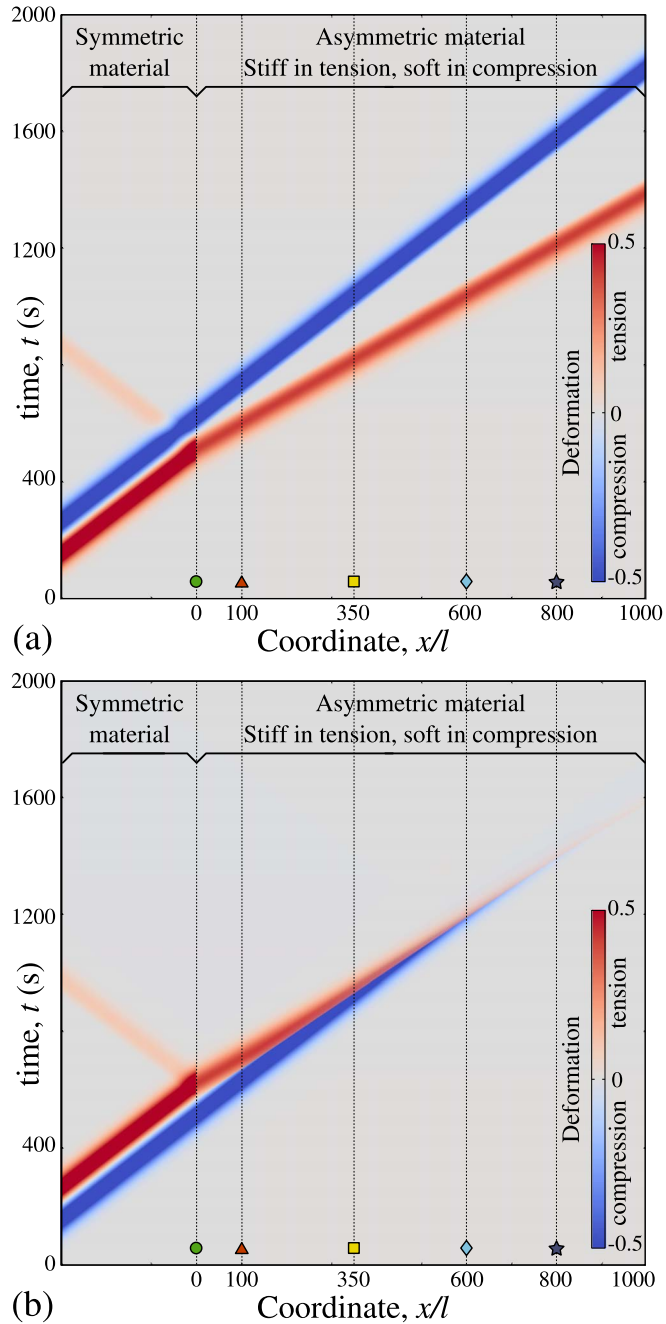


Figure 4. Simulation results for $\alpha = 0.3$, $\mu/\rho = 0.01 \text{ m}^2/\text{s}$, $E/\rho = 1 \text{ m}^2/\text{s}^2$: (a) and (b) represent spatio-temporal deformation map (u_x) and correspond to the diagram (a) and (b) in Figure 3, respectively; $x/l = 0$ separates symmetric and asymmetric segments.

Note that contrary to the study of [36], thanks to absorbing layers, there is no additional waves interacting with the shock front. The overlap process creates a discontinuity in deformation (shock) and thus leads to emergence of high-frequency oscillations and accompanying viscous

dissipation, which results in partial or almost complete annihilation of tensile and compressive wave components (see Figure 4(b)). However, these oscillations do not necessarily imply high-frequency alteration between tension and compression. In the first stage, high-frequency oscillations superpose with the compressive wave.² The nature of these oscillations, which cannot be removed through a time-step refining, is still to be investigated in detail. Since in Kelvin–Voigt model the amplitude of a wave with a real wavenumber k decays in time t as $\exp(-\mu k^2 t/2\rho)$; in the limit of high wavenumber $k > 2c^\pm/\mu$, the waves are overdamped and the harmonic part fully disappears. At later stages, the oscillations produced by the overlap of tensile and compressive components lead to frequent alteration of the deformation sign. As known from [53, 54], oscillators with piecewise-smooth characteristics possess sub-harmonic resonances at higher frequencies, which ensure relatively high amplitude and enhanced dissipation.

It is straightforward to find an approximate propagation distance L_o needed for the tensile and compressive parts of initially harmonic signal to superpose completely. We introduce the following notations:

$$E_{\max} = \max\{E^+, E^-\}, \quad E_{\min} = \min\{E^+, E^-\}$$

and

$$c_{\max} = \max\{c^+, c^-\}, \quad c_{\min} = \min\{c^+, c^-\},$$

the material contrast is then denoted by

$$\gamma = E_{\max}/E_{\min} = (1 + |\alpha|)/(1 - |\alpha|) > 1$$

and

$$c_{\max}/c_{\min} = \sqrt{\gamma}.$$

The overlap distance depends on wave speeds in the bimodular segment, on the amplitudes and the initial separation in time of tensile and compressive components, which is equal to a half of the period $\Delta T = \pi/\omega_0$ in the symmetric segment (where the oscillations are forced). Equating the length needed for faster and slower waves to travel to the same spatio-temporal point and requiring the full-period overlap, we obtain the overlap distance

$$L_o = \frac{2\pi c_{\max}}{\omega_0(\sqrt{\gamma} - 1)}. \quad (4)$$

The full geometrical overlap is needed because, as will be shown later, the speed of the shock separating compressive and tensile components for equal amplitude waves, travels at the speed in the interval between the two components. A detailed study of the shock wave speed for the different cases could be found in [36, 39], some preliminary considerations are provided in Section 9. It would be important to remark here that in the pioneering paper [34] different types of particular points x^* were introduced: (1) α (shocks) for which $\varepsilon(x^*+) \varepsilon(x^*-) < 0$, (2) β (signotons) for which $\varepsilon(x^*+) = \varepsilon(x^*-) = 0$ but $\varepsilon(x)$ changes its sign when crossing $x = x^*$, (3) γ (semi-signotons) and $\varepsilon(x^*+) \varepsilon(x^*-) = 0$ but $\varepsilon(x^*+) \neq \varepsilon(x^*-)$ and ε changes its sign³ when crossing $x = x^*$ and (4) δ (simple discontinuity) for which $\varepsilon(x^*+) \varepsilon(x^*-) > 0$ and $\varepsilon(x^*+) \neq \varepsilon(x^*-)$. If the symmetric segment is stiff $c_0 = c_{\max}$, then the overlap distance is given by

$$L_o = \lambda_0 / (\sqrt{\gamma} - 1);$$

if $c_0 = c_{\min}$ then

$$L_o = \lambda_0 + \lambda_0 / (\sqrt{\gamma} - 1).$$

²Note that these oscillations do not emerge if tensile and compressive waves going in opposite directions pass through each other.

³In the current work even if the value of $\varepsilon = 0$ on one of the sides, we will call this point semi-signoton or stable semi-signoton in contrast to the classical one, which is unstable.

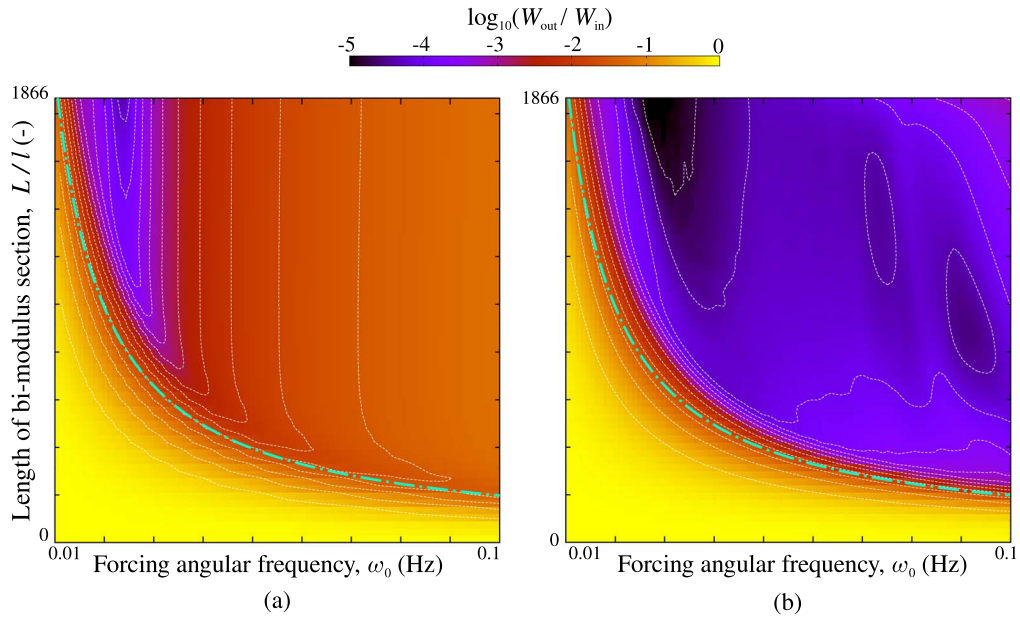


Figure 5. The decimal logarithm of the ratio of transmitted to incident energy is plotted for different forcing frequencies ω_0 and different lengths of bimodular segment L : (a) Configuration 1 (see Figures 2(a), 3(b)), (b) Configuration 2 (see Figures 2(b), 3(c)). Dashed curves mark transmission iso-levels, dash-dotted curves represent (4).

6. Energy-absorbing properties

The high-frequency cascades emerging in annihilation of tensile and compressive waves present a powerful dissipative or energy-absorbing mechanism. To test its properties we analyse the energy passing through the bimodular segment(s) as a function of its length and forcing frequency ω_0 . The injected energy is computed as the work of the forcing

$$W_{in} = \frac{1}{2} \int_0^T f(t) u_{,t} dt, \tag{5}$$

where T is the forcing time. The factor 1/2 appears here since only half of the energy goes towards the bimodular segment, the other half goes to the left towards the absorbing layer. The transmitted energy W_{out} is computed right after the bimodular segment(s) (see detectors in Figure 1); it is computed as the energy passing through a point x_d and computed as:

$$W_{out} = A \int_0^{T_{sim}} \left[\rho \left(\frac{\partial u}{\partial t} \right)^2 + E \left(\frac{\partial u}{\partial x} \right)^2 \right] \Big|_{x=x_d} c_0 dt, \tag{6}$$

where A is the area of the section, c_0 is the wave velocity in the symmetric segment and x_d is the location of the detector. The time interval $[0, T_{sim}]$ spans the entire duration of the simulation to grasp all waves and most of reflections excited by incident waves. Because of the absorbing layer on the far-right end of the structure, the energy integrated over time is equal to the energy passed from left to right within the given time interval. The calculation of the injected energy W_{in} is also verified by the same calculations for a detector located prior to the bimodular segment(s), which slightly differ from the accurate (5), because (6) accounts for the reflected waves from the interfaces.

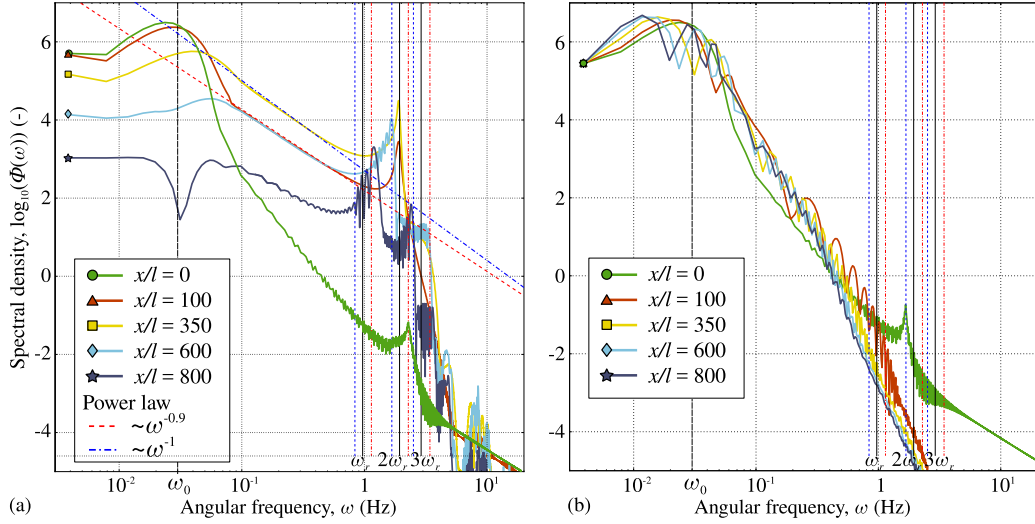


Figure 6. Spectral density $\Phi(\omega)$ at locations marked in Figure 4(b). (a) Configuration 1, scenario of Figure 3(b). Initial peak at the incident frequency ω_0 is visible, as well as an emerging high-frequency peak at sub-resonance frequency $2\omega_r$. Energy cascade with an exponent in the interval $[0.9, 1]$ is highlighted. (b) The spectral density remains almost unchanged for Configuration 1 and scenario of non-overlapping tensile and compressive wave components, see Figures 3(a), 4(a).

The logarithm of the ratio of transmitted to incident signal energy $\log_{10}(W_{\text{out}}/W_{\text{in}})$ is plotted in Figure 5(a,b) as a function of the forcing frequency ω_0 and the length of the bimodular segment L , for Configurations 1 and 2, respectively. The following parameters were used $E/\rho = 1$ (m^2/s^2), elemental cell length is $l = 1$ (m), section area $A = 1$ (m^2), $\alpha = 0.3$, $\mu/\rho = 0.01$ (m^2/s). For Configuration 1, the transmitted energy reduces significantly if the length of bimodular segment is greater than the overlap length L_o given in (4). For Configuration 2 (see the scheme in Figure 3(c)), the same qualitative effect is observed, however, it is greatly amplified⁴ by the bimodular segment of the same length L but with the opposite asymmetry, which is introduced right after the first bimodular segment. After the first (partial) annihilation of tensile and compressive waves, the remnants of the tensile component precedes the compressive ones. The second segment with the inverse asymmetry serves to collide them again and dissipate their energy. Multiple combinations of antisymmetric segments can be used to ensure even more efficient damping as long as within every segment tensile and compressive components overtake each other, i.e. the length of the segment is greater than the overlap length $L \geq L_o$ (see (4)). From (4) and the simulation data it follows that the absorption is very efficient for high and low frequencies as long as the following condition is met:

$$\omega_0 \geq \frac{2\pi c_{\text{max}}}{L(\sqrt{\gamma} - 1)}. \quad (7)$$

A comparable damping mechanism occurs for a random wave packet, which contains a roughly equal proportion of tensile and compressive components which “annihilate” via the same mechanism. It will be investigated in detail in Section 8.

⁴In average, the double layer enables to absorb energy in such a way that the remaining energy is two orders of magnitude less than in the case of a single layer.

7. Spectral analysis

Presence of high-frequency energy cascades can be shown through spectral analysis. In Figure 6 the evolution of the spectral density of deformation $u_{,x}$ is shown for the cases depicted for the simulations presented in Figure 4. The power spectral density is computed at several locations x along the bimodular segment (marked with dashed lines equipped with a marker in Figure 4) for the whole time history as $\Phi(\omega, x) = \hat{u}_{,x} \hat{u}_{,x}^*$, where

$$\hat{u}_{,x}(\omega, x) = \int_0^{T_{\text{sim}}} e^{-i\omega t} u_{,x}(x, t) dt$$

is the temporal Fourier transform, where $\hat{\bullet}^*$ denotes the conjugate value, and ω is the angular frequency. We assume that at $t < 0$ and $t > T_{\text{sim}}$ the studied system is at rest. The system is forced mainly at frequency $\omega_0 = 0.03$ Hz, resulting in a smooth peak in Φ for the signal entering the bimodular segment at $x = 0$. Note that the resonance frequencies of the bimodular element is given by

$$\omega_r = \frac{2j\sqrt{1-\alpha^2}\sqrt{E_0/\rho}}{l(\sqrt{1-\alpha} + \sqrt{1+\alpha})}$$

(see, [55]), where the main resonance occurs for $j = 1$ and high-frequency sub-harmonic resonances occur at $j > 1, j \in \mathbb{N}$. In the signal spectrum (Figure 6(a)) for the case of wave overlap (Figure 4(b)), a second peak emerges at $j = 2$ sub-harmonic frequency of elemental cells. This peak, which grows with the propagation distance, presents a sink for the energy transmitted from low frequencies. The energy spectrum thus contains two peaks connected via a power law decay segment with the exponent between -1.0 and -0.9 as shown in Figure 6(c). Note that the energy decay of the main frequency ω_0 , as well as the rise and subsequent decay of sub-frequencies $n\omega_0$, for $n \in \mathbb{N}, n > 1$ is consistent with the findings presented in [37], where the authors grasped the main features of this dissipation mechanism. In contrast, when tensile and compressive components separate (Figures 3(a) and 4(a)), the spectrum depicted in Figure 6(b) does not present any particularities and the energy spectrum remains stable.

8. Random incident wave packet

Here, we consider a random incident wave packet containing many harmonics but compact in space and time. The wave packet is induced by a force which follows a nominal self-affine evolution localized in time/space:

$$f(t) = \exp\left(-\frac{(t-t_0)^2}{\sigma_i^2}\right) \sum_{k=k_l}^{k_h} A_k \left(\frac{k}{k_l}\right)^{-(0.5+H)} \sin\left(\frac{2\pi kt}{T_i} + \varphi_k\right), \tag{8}$$

where A_k is a random amplitude given by $A_k = 1 + 0.2r_k$ (N), where $r_k \in [-1, 1]$ is a random variable with a uniform probability density; $\varphi_k \in [0, 2\pi]$ is a random phase which is also selected from a uniform distribution, k_l is the lower summation number and represents a normalized lower cut-off wavenumber, $k_h > k_l$ is the upper summation limit and represents the upper cut-off wavenumber, so $k_h - k_l$ is the number of modes present in the signal, σ_i (s) determines the duration of the signal and t_0 is the centred signal time, T_i is the basic period and is selected to be $T_i = 4\sigma_i$ to avoid repetition of patterns in the incident signal; $0 < H < 1$ is the Hurst exponent controlling the self-affinity, so the spectrum of the signal follows a power law decay $\langle \Phi_k \rangle \sim k^{-(1+2H)} = k^{-(5-2D_f)}$, where the average $\langle \bullet \rangle$ represents the ensemble average and $D_f = 2 - H$ is the fractal dimension, $D_f \in [1, 2]$. Examples of random wave packets and their spectra are shown in Figure 7. Because of the viscous dissipation in the system, to study the effect of bimodular segments, one has to select such parameters for the incident signal so that in the absence of

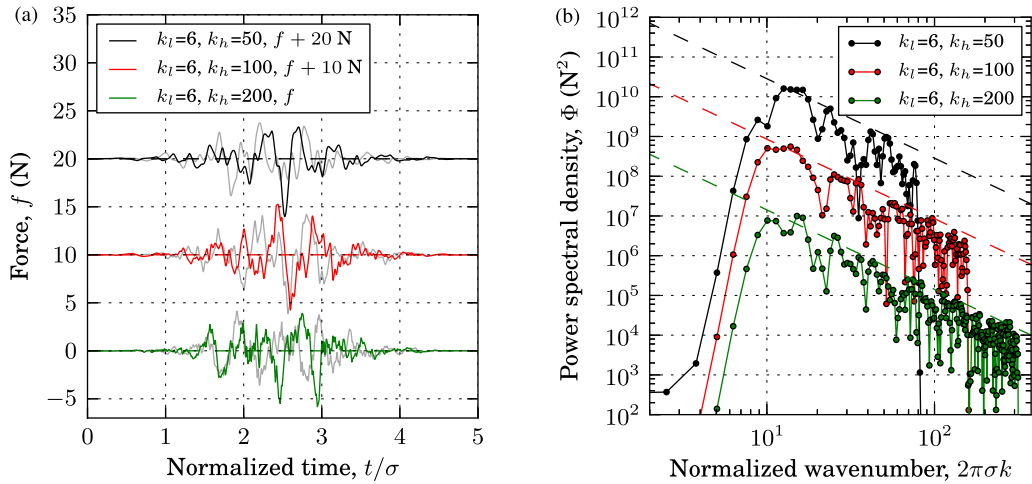


Figure 7. Examples of random self-affine force used to generate incident wave packets according to (8): (a) generated forces for $k_l = 6$ and $k_h = \{50, 100, 200\}$ and $H = 0.5$ are presented, two random realizations are shown for every combination of parameters; (b) the corresponding power spectral densities of the coloured signals, to guide the eye, dashed curves show a power law $\sim k^{-(1+2H)}$. For representation purpose, the plots are shifted in Y axis.

Table 1. Parameters used in simulation of a transmission of a random incident wave packet, see (8) for notations

Parameter	Notation	Value	Units
Signal lower cut-off	k_l	6	—
Signal higher cut-off	k_h	100	—
Standard deviation	σ_i	1000	s
Basic period	T_i	4000	s
Central time	t_0	3000	s
Hurst exponent	H	0.5	—
Elastic contrast	α	$[-0.3, 0.3]$	—
Kinematic viscosity	μ/ρ	0.003	m^2/s
Reduced stiffness of symmetric layer	E_0/ρ	1	m^2/s^2
Reduced tension stiffness in first meta-segment	E^+/ρ	1	m^2/s^2
Simulated normalized length	L/l	20,000	—
Simulated time	T	30,000	s
Time step	dt	0.2	s

such a segment, the signal passes through the entire system without significant filtering of high-frequency modes. The selected parameters are summarized in Table 1, for such parameters the ratio of transmitted to injected energy measured at the two detectors is $W_{\text{out}}/W_{\text{in}} \approx 0.93$; the signal at detector 2 is compared with the signal at detector 1 in Figure 8 for $\alpha = 0$, other parameters remain the same as in Table 1. The simulation domain and its duration are kept rather large because of the rich content of the signal.

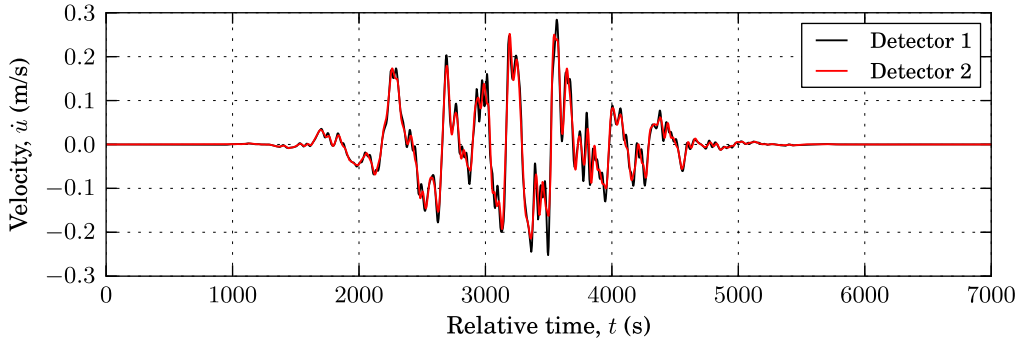


Figure 8. The velocity at detector 2 is compared with the velocity at detector 1 to visualize how the signal changes after passing through the simulation domain due to viscous dissipation but in absence of the elastic contrast, i.e. $\alpha = 0$. The signal at detector 2 is shifted by 19,053 s to superpose with the signal at detector 1. The corresponding ratio of signal energies is $\approx 93\%$.

8.1. Transmission of energy

In Figure 9(a) we plot the energy ratio W_{out}/W_{in} (transmission factor) as a function of bimodular length L for Configuration 1 (without second segment with the opposite asymmetry) and different elastic contrasts α . As seen from the figure, all the data could be described by the same function with an exponential decay (to a certain positive limit) with respect to the length of the bimodular segment raised to the power of $3/2$:

$$\mathcal{T}(L) = \frac{W_{out}}{W_{in}} = \mathcal{T}_{min} + (\mathcal{T}_{max} - \mathcal{T}_{min}) \exp(-(L/L_*)^{3/2}), \tag{9}$$

where $\mathcal{T}_{min}, \mathcal{T}_{max}$ are the minimal and the maximal values obtained for saturated transmitted energy and transmitted energy in absence of bimodular segment, respectively; L_* is the characteristic length which characterizes the reduction in transmitted energy. However, it would be reasonable to suggest a renormalization of the bimodular-segment length in order to account for the difference in elastic moduli used for positive and negative values of α : the characteristic length of intersection would scale as $L \sim c^{max} - c^{min}$, therefore it would be reasonable to plot the transmission factor with respect to the renormalized bimodular length L'

$$L' = \begin{cases} \frac{L}{l} \frac{2}{1 - \sqrt{(1-\alpha)/(1+\alpha)}}, & \text{if } \alpha > 0, \\ \frac{L}{l} \frac{2}{\sqrt{(1+\alpha)/(1-\alpha)} - 1}, & \text{if } \alpha < 0. \end{cases}$$

The mean value of the transmission factor and the error bars (root-mean-square deviation) are obtained for 10 simulations carried out for different realizations of the incident signal (see Supplementary material [65]). Contrary to a mono-harmonic signal, for a random wave packet the transmission factor cannot be reduced below $\approx 10\%$ because of eventual full elimination of either tensile or compressive wave components, so that the remaining component, accordingly compressive or tensile, persists. In order to obtain a more precise expression, it would be reasonable to take into account the reflected part of the signal, i.e. the part of the signal that does not travel through the bimodular segment, so the ultimate form of the transmission factor with the normalization of the bimodular-segment length takes the form:

$$\mathcal{T}'(L') = \frac{W_{out} + W_{refl}}{W_{in}} = \mathcal{T}'_{min} + (\mathcal{T}'_{max} - \mathcal{T}'_{min}) \exp(-(L'/L'_*)^{3/2}) + \frac{W_{refl}}{W_{in}}. \tag{10}$$

The last term can be estimated as $W_{\text{refl}}/W_{\text{in}} \approx (1 - 2/(1 + \sqrt{(1-\alpha)/(1+\alpha)}))^2$ for $\alpha < 0$, for $\alpha > 0$ the reflected waves have a much smaller energy and can be neglected. Even for the negative α , the value of the reflected energy is relatively small as could be seen in Figure 9(a) as the shift between curves in the asymptotic limit of $L \rightarrow 0$. Note that this simplification (10) is possible because the reflected energy is independent of the length of bimodular segment. The transmission factor taking into account the reflected energy \mathcal{T}' is shown in Figure 9(b) and the relevant normalization of the bimodular-segment length L' allows to collapse all the data points on a single master curve with the following parameters: fixed $\mathcal{T}'_{\text{max}} = 0.93$ and those obtained by the mean least square fit $\mathcal{T}'_{\text{min}} = 0.1128$, $L'_* = 438.37$.

8.2. Signal change

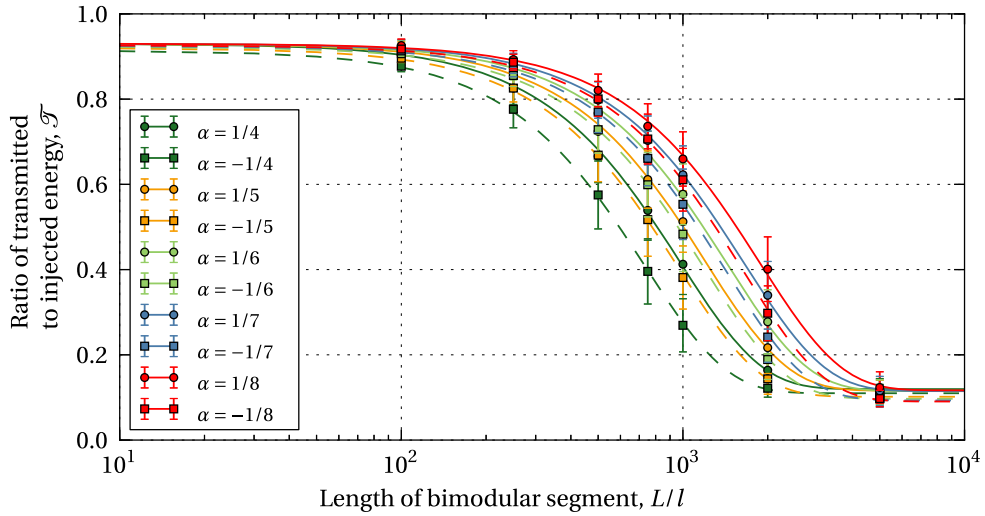
Apart from the reduction in the transmitted energy, it is important to understand how the shape of the velocity signal changes after passing through the bimodular segment. In Figure 10 we show examples of the input and output signal for the length of bimodular segment $L/l = 5000$ and $\alpha = \pm 1/4$. The most evident observation is the change in standard deviation σ and average “sign” of the signal. For $\alpha > 0$ the output signal contains rather negative velocities, and vice versa, for $\alpha < 0$ the signal contains rather positive components. This change is important to understand the energy absorption in the bimodular segment, because such trend in converting the signal into purely mono-sign signal does not permit further overlap and annihilation, moreover, this “sign-polarization” results in a net motion to the right or to the left of the entire system.

The “sign” of the signal can be characterized by skewness of the distribution $\tilde{\mu}_3 = \mu_3/\sigma^3$, where μ_3 is the third moment of the probability distribution. For our data, the distributions are computed over an input signal in the window of $t \in [0, 7\sigma_i]$ and for the output signal in $t \in [t_{\text{max}} - 3.5\sigma, t_{\text{max}} + 3.5\sigma]$, where t_{max} corresponds to the $\max|u|$ of the output signal. The standard deviation of the signal reduces by a factor of three, and the skewness becomes considerably positive for negative α and vice versa, i.e. the skewness is negative for positive α , see Table 2(a). For $L/l = 5000$ the dependence on the level of elastic contrast α is quite marginal, whereas for shorter lengths, for example, $L/l = 1000$ this dependence becomes pronounced since such a length is not sufficient to ensure overlap of positive and negative parts, see Table 2(b). Note that in the Configuration 2, in presence of the segment of the inverse asymmetry, the skewness remains almost the same and the standard deviation is slightly reduced by $\approx 12.5\%$. In Figure 11 we show velocity probability densities of the incident signal and of the output signal which passed through the bimodular of length $L/l = 5000$, the data are shown for different values of the elastic contrast α . Note that incident signals are the same for different α , the small difference in probability density functions (PDF) is explained by different reflections from the bimodular interface.

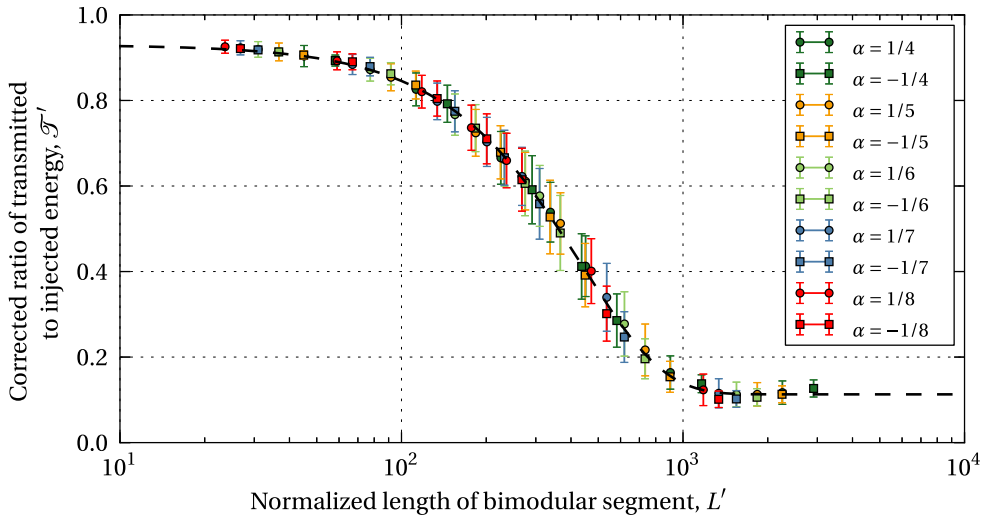
9. Geometrical model

A simple geometrical explication could be given to the observed decrease in the transmitted energy. Let us consider a wave packet in a symmetric non-dispersive medium travelling to the right at wave speed c_0 as a superposition of the positive and negative parts $u_{,x}(x - c_0 t) = \langle u_{,x}(x - c_0 t) \rangle - \langle -u_{,x}(x - c_0 t) \rangle$, where $\langle x \rangle = \max\{0, x\}$, within the bimodular segment the speed of propagation for these parts would be different, moreover, the positive and negative parts will change due to their gradual superposition accompanied by energy cascades:

$$u_{,x}(x, t) = \langle u_{,x}(x - c_0 t, t) \rangle - \langle -u_{,x}(x - c_0 \sqrt{(1-\alpha)/(1+\alpha)} t, t) \rangle,$$



(a)



(b)

Figure 9. (a) Transmission factor \mathcal{T} (ratio of transmitted to injected energy) is plotted with respect to the length of the bimodular segment L for different elastic contrasts α ; the curves represent (9) with parameters identified by the mean least square fit, dashed curves correspond to $\alpha < 0$, solid curves to $\alpha > 0$. (b) Transmission factor taking into account reflected energy \mathcal{T}' and plotted with respect to the normalized length of the bimodular segment L' , the master curve represent (10) with parameters identified by the mean least square fit; the same data points as in (a) are plotted; the points represent the average data computed over 10 realizations and the error bars are equal to the standard deviation.

by changing the variable $x' = x - c_0 t$ and introducing new notations $\varphi(x', t) = \langle u_{,x'}(x', t) \rangle$ and $\psi(x' - \Delta c t, t) = -\langle -u_{,x'}(x', t) \rangle$, where $\Delta c = c_0(\sqrt{1 - \alpha})/(1 + \alpha) - 1$, we obtain the following equa-

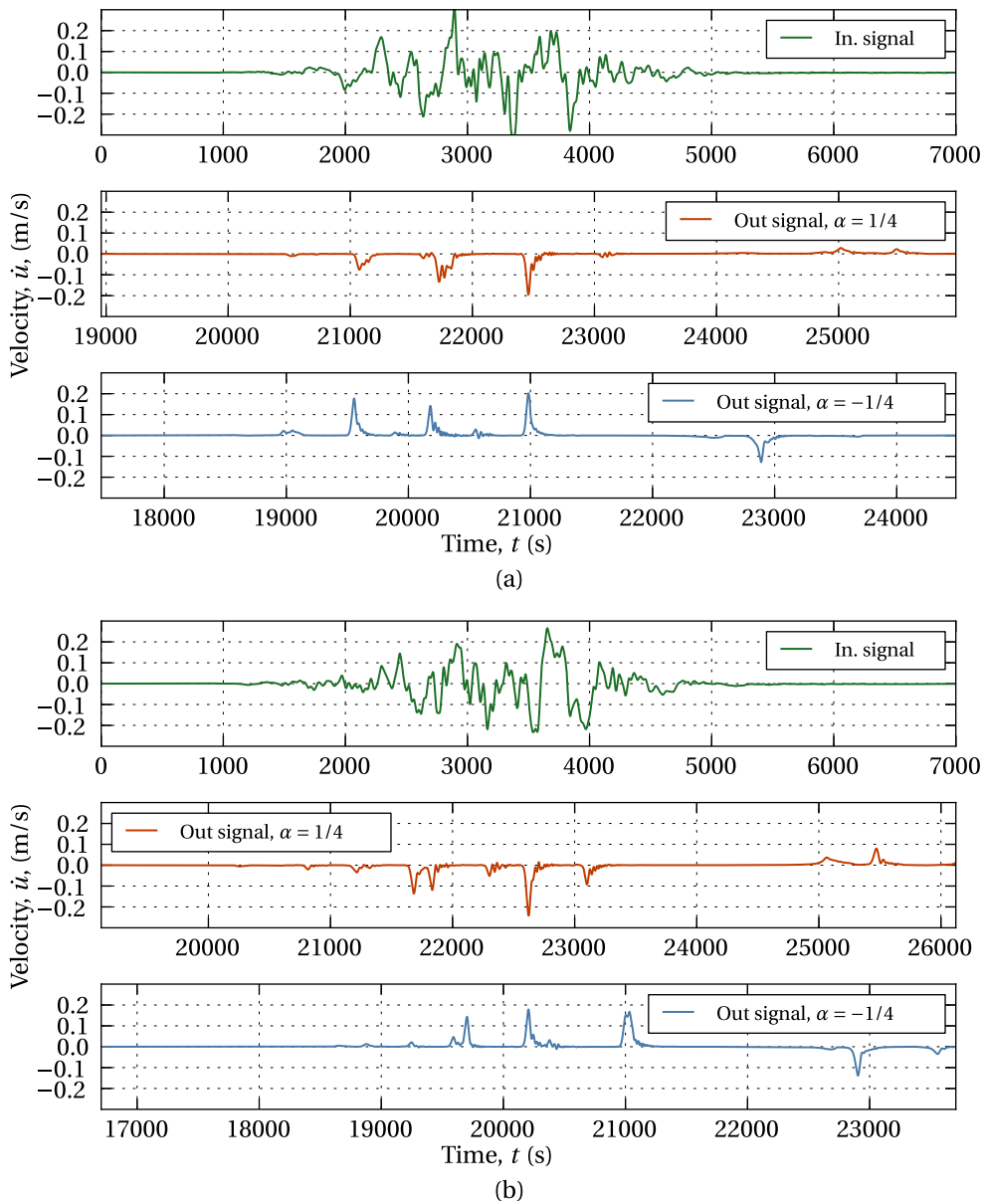


Figure 10. Illustration of signal's change for two random realizations. The incident signal (upper panels in (a,b)) deforms passing through the bimodular segment of length $L/l = 5000$ and takes the form of sign-polarized signal with mainly positive components for $\alpha > 0$ and negative components for $\alpha < 0$, see middle and lower panels in (a,b).

tion to represent the signal:

$$u_{,x'}(x', t) = \varphi(x', t) + \psi(x' - \Delta ct, t),$$

of course, far from discontinuity point (shock), i.e. the points $x'^*(t)$ at which the function changes sign $u_{,x'}(x'^*+, t)u_{,x'}(x'^*- , t) < 0$, functions φ and ψ preserves their form, i.e. their time derivatives

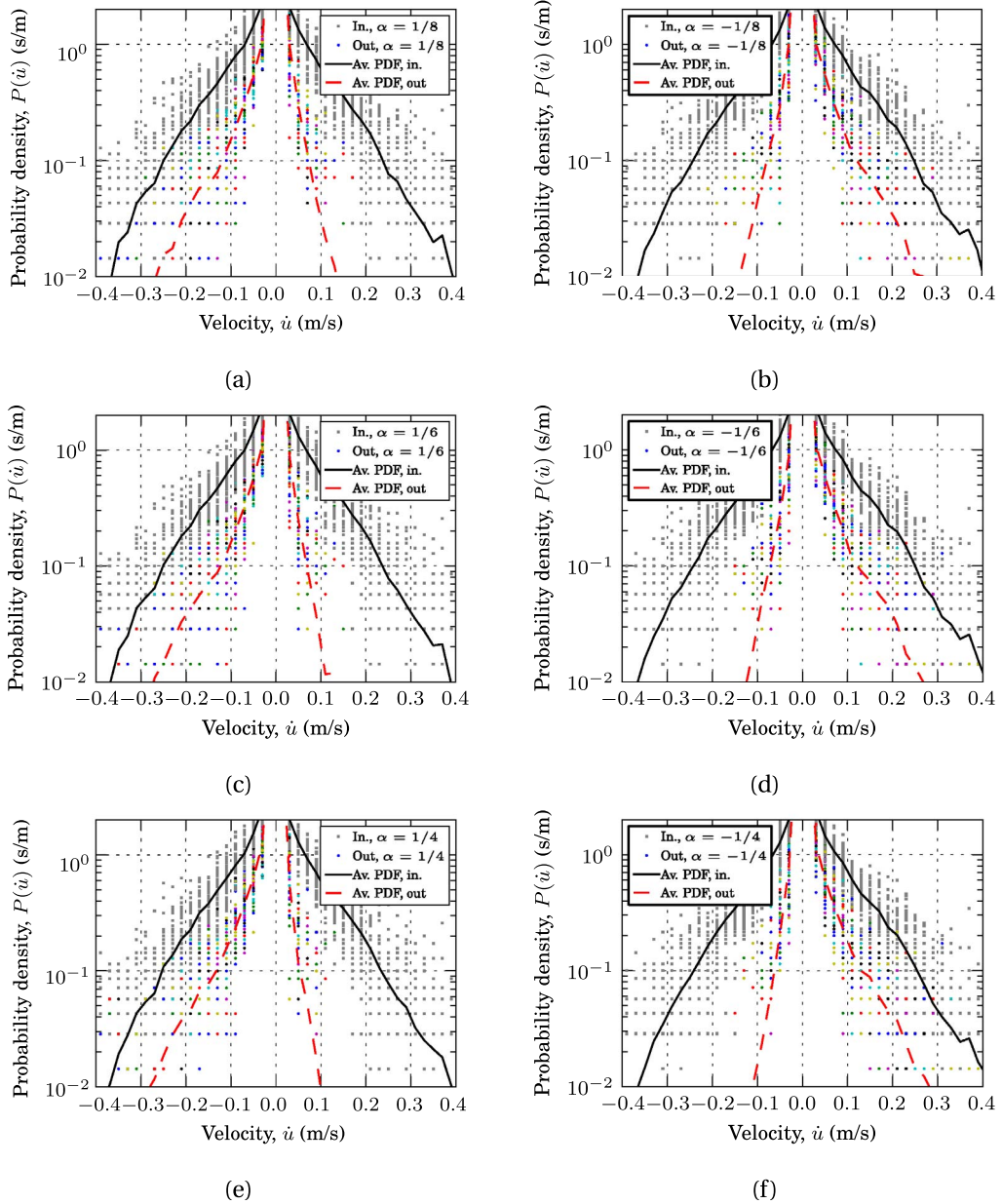


Figure 11. PDF of velocities of the incident signal and of the output signal which passed through the bimodular segment of length $L/l = 5000$, individual points represent PDF values of a particular test and the curves are the average data computed over 50 realizations, both distributions are computed over 50 bins: (a,b) $\alpha = \pm 1/8$, (c,d) $\alpha = \pm 1/6$, (e,f) $\alpha = \pm 1/4$. All the data are available in Supplementary material [65].

Table 2. Averaged standard deviation and skewness of the input and output signals for different values of α and for (a) $L/l = 5000$ averaged over 50 realizations, (b) $L/l = 1000$ averaged over ten realizations

α	Input signal		Output signal	
	Std σ	Skewness $\tilde{\mu}_3$	Std σ	Skewness $\tilde{\mu}_3$
-1/4	0.0634	0.1882	0.0214	5.2150
-1/5	0.0631	0.1579	0.0210	4.9662
-1/6	0.0630	0.1399	0.0207	4.7409
-1/7	0.0623	-0.1475	0.0210	4.4319
-1/8	0.0628	0.1184	0.0206	4.3772
1/8	0.0622	-0.0146	0.0205	-5.0246
1/7	0.0620	-0.2617	0.0193	-4.6584
1/6	0.0621	-0.0355	0.0208	-5.2974
1/5	0.0621	-0.0525	0.0212	-5.4514
1/4	0.0620	-0.0803	0.0216	-5.8283
(a) $L/l = 5000$				
-1/4	0.0627	-0.0225	0.0397	0.8776
-1/5	0.0626	-0.0600	0.0443	0.4105
-1/6	0.0625	-0.0836	0.0470	0.1804
-1/7	0.0624	-0.1011	0.0489	0.0718
-1/8	0.0623	-0.1139	0.0503	0.0239
1/8	0.0620	-0.2894	0.0486	-0.7302
1/7	0.0620	-0.2979	0.0462	-0.7522
1/6	0.0620	-0.3085	0.0432	-0.9362
1/5	0.0621	-0.3222	0.0383	-1.3727
1/4	0.0621	-0.3406	0.0320	-2.0355
(b) $L/l = 1000$				

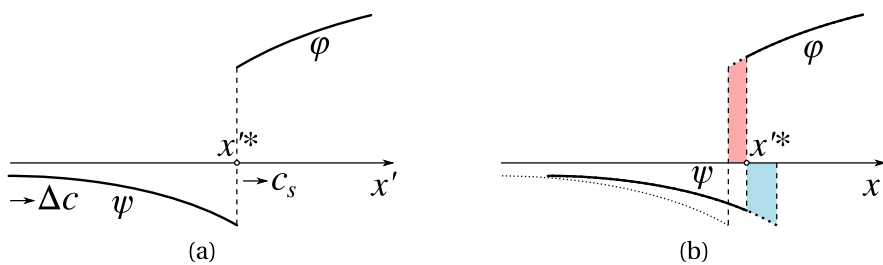


Figure 12. Motion of a α -discontinuity (shock) x'^* at speed c_s in coordinate system at which the positive part φ remains at rest: configuration (a) at t_0 and (b) at $t_0 + \Delta t$, dotted lines represent the signal at time t_0 . Dashed areas under the curves for slowly varying φ and ψ and for $\Delta t \rightarrow 0$ are given by $\varphi(x'^*)c_s \Delta t$ for the tensile part (reddish one) and $|\psi(x'^*)|(\Delta c - c_s) \Delta t$, these areas are equal and they correspond to the deformation amplitude loss.

take the form $\varphi_{,t} = 0$ and $\psi_{,t} = -\Delta c \psi_{,x'}$. However, at α -discontinuity (shock) the signal loses some

amplitude following (see Figure 12):

$$\int_{-\infty}^{\infty} u_{,x't} dx = 2\Delta c \sum_{x'^*} \frac{\varphi(x'^*)|\psi(x'^*)|}{\varphi(x'^*) + |\psi(x'^*)|},$$

where the sum is over all α discontinuities (following the terminology of [34]) and it always holds that $\varphi \geq 0$ and $\psi \leq 0$. This result could be obtained by simple geometrical interpretation sketched in Figure 12 for an α -discontinuity moving at speed c_s : if we assume small change of deformation at distance $c_s \Delta t$, i.e. $|\varphi(x) - \varphi(x + c_s \Delta t)| \ll 1$ and $|\psi(x) - \psi(x - c_s \Delta t)| \ll 1$ then in the course of its propagation from instance t_0 to instance $t_0 + \Delta t$, the α -discontinuity will release the integral of deformation of the positive part given by $c_s \varphi(x'^*) \Delta t$ which appears to be equal to the lost deformation of the negative part $|\psi(x'^*)|(\Delta c - c_s) \Delta t$. By equating these two terms the speed of the α -discontinuity c_s can be found, it depends on the asymmetry of the jump and in the moving coordinate system x' it is given by:

$$c_s(x'^*) = \Delta c \frac{|\psi|}{\varphi + |\psi|} \Big|_{x'=x'^*}.$$

To obtain its absolute speed, one needs to simply add c^+ speed. As follows from this equation, the speed of the α -discontinuity can be non-constant even though the positive and negative parts propagate at constant speeds. For equal values of φ and ψ , the speed of the α -discontinuity is simply $c_s = \Delta c/2$, which was used in Section 5 to deduce the full overlap distance. The squared values of all deformation losses with a Young's modulus factor and integrating them in time and in section A would give us the total loss in potential energy predicted by this simplified geometric model:

$$W_{\text{loss}}(t) = \frac{A(E^+ + E^-)}{2} \Delta c \int_0^t \sum_{x'^*(t')} \left(\frac{\varphi(x'^*)\psi(x'^*)}{\varphi(x'^*) + |\psi(x'^*)|} \right)^2 dt'. \tag{11}$$

Even though this equation is not easy to use with a random signal, it could serve to obtain an asymptotic solution for small overlaps, it could be also helpful for a numerical treatment or for the analysis of simple signals.

Let us consider, for example, a signal $\varphi = \langle a^+ \sin(k(x - c^+ t)) \rangle$ and $\psi = -\langle -a^- \sin(k(x - c^- t)) \rangle$, values of φ and ψ at α -discontinuity in the moving coordinate system $x' = x - c^+ t$ will be:

$$\varphi(x'^*, t) = a^+ \sin(kx'^*), \quad \psi(x'^*, t) = -a^- \sin(k(\Delta c t - x'^*)), \quad x'^* = \int_0^t c_s(t) dt$$

then the following integral equation can be formulated for the α -discontinuity speed:

$$c_s(t) = \Delta c \frac{a^- \sin(k(\Delta c t - x'^*))}{a^- \sin(k(\Delta c t - x'^*)) + a^+ \sin(kx'^*)}, \quad x'^* = \int_0^t c_s(t) dt$$

which greatly simplifies for $a^+ = a^- = a$ because in this case $c_s = \Delta c/2$ and

$$\varphi(x'^*, t) = a \sin(k\Delta c t/2) = -\psi(x'^*, t).$$

For this simple case (see Figure 13(a)) the energy loss per one α -discontinuity would be given by:

$$W_{\text{loss}}(x'^*, t) = \Delta c \frac{A(E^+ + E^-) a^2}{4} \int_0^t \sin^2(k\Delta c_s t) dt' = \frac{A(E^+ + E^-) a^2}{8} \left(L - \frac{\sin(kL)}{k} \right),$$

which results in the following evolution of the energy loss reformulated in length of the bimodular layer following $L = \Delta c t = 2c_s t$ and expressed as the remaining energy normalized by the initial energy ($W_0 - W_{\text{loss}}(L) / W_0$):

$$1 - \frac{W_{\text{loss}}(L)}{W_0} = \begin{cases} 1 - \frac{kL - \sin(kL)}{2\pi}, & \text{if } L < 2\pi/k \\ 0, & \text{otherwise.} \end{cases} \tag{12}$$

In Figure 13(a) the evolution of the signal within this simplified geometrical model is shown for the case $a^+ = a^-$ (see Supplementary material [65] for the code). In this case the signal fully

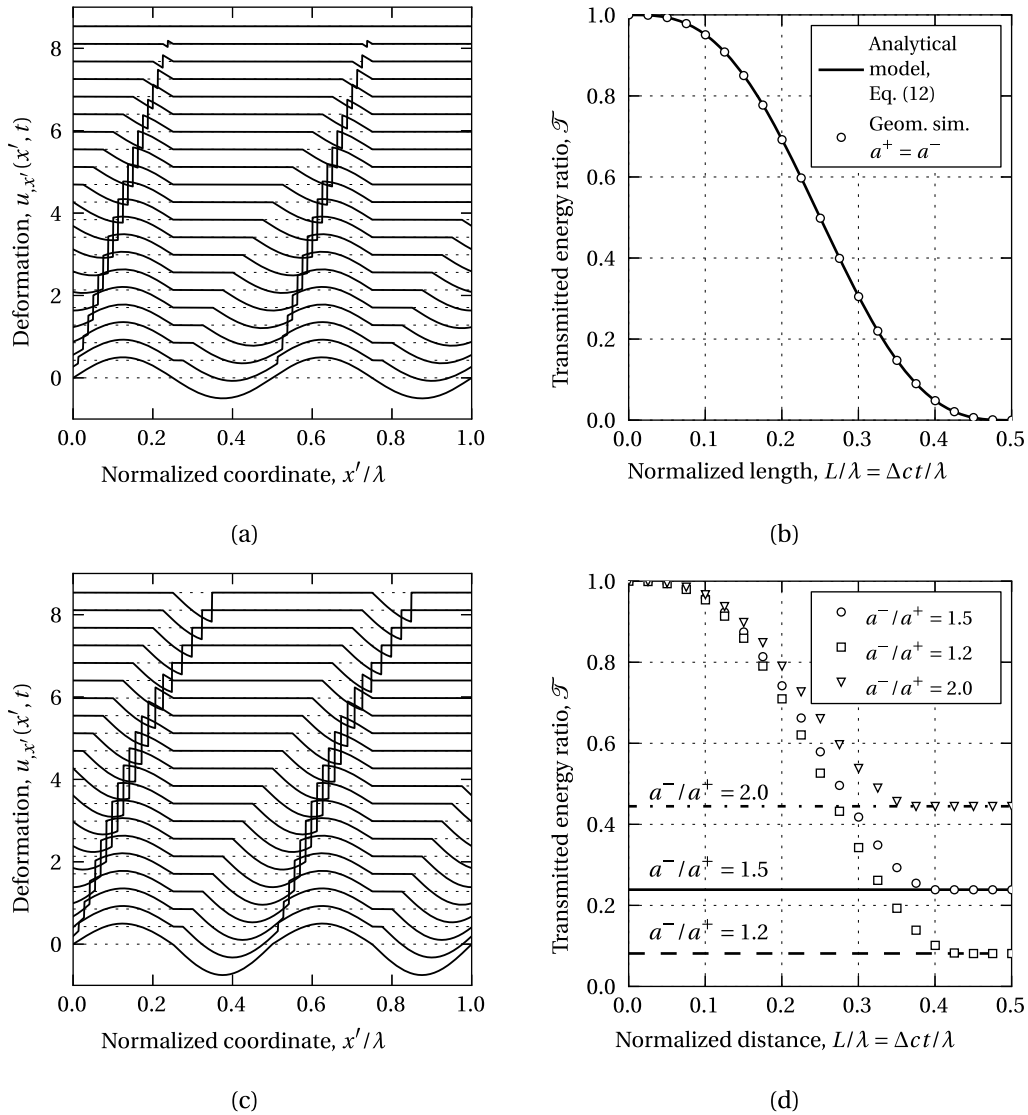


Figure 13. Evolution of the deformation signal $u_{x'}(x', t)$ in time in the reference coordinate system x' moving at speed c^+ , this evolution is simulated with a geometrical overlap model for (a) $a^+ = a^-$ and (c) for $a^-/a^+ = 1.5$; the remaining parameters are $\rho = 2 \text{ kg/m}^2$, $E^+ = 1 \text{ Pa}$, $E^- = 2 \text{ Pa}$, $c^+ = 1/\sqrt{2} \text{ m/s}$, $c^- = 1 \text{ m/s}$, $\Delta c = 1 - 1/\sqrt{2} \text{ m/s}$, $\lambda = 1 \text{ m}$, $k = 4\pi/\lambda$, $dt = \lambda/(N\Delta c)$, where $N = 4000$ is the spatial discretization. Every snapshot taken every 100 time steps dt is shifted vertically by the value of $500dt$. In (b) and (d) the evolution of the remaining potential energy in the signal compared to the initial energy is computed using the geometrical overlap model and compared with analytical solution (12) in (b); in (d) solid, dashed and dash-dotted lines represent the remaining energy computed by (14).

disappears. The evolution of the transmitted energy is shown in Figure 13(b) and compared with (12). In case when $a^+ \neq a^-$ (Figure 13(c)), the evolution of the energy loss is not easy to compute, but the remaining energy can be readily computed. The integral deformation for the considered case is given as $2a^\pm/k$ for positive and negative parts of a single wave, so the absolute

value of their difference is $2|a^- - a^+|/k$ which is nothing but the remaining integral deformation of the part with the greater amplitude, say $a^- > a^+$, i.e.

$$\int_0^y a^- \sin(kx') dx' = 2(a^- - a^+)/k,$$

where a non-zero signal will remain only within the intervals $[0 + 2\pi, y + 2\pi]$. From this equation, we can find the value of y as:

$$y = \frac{1}{k} \arccos(2a^+/a^- - 1). \quad (13)$$

Therefore, the remaining energy per wavelength will be given by

$$1 - \frac{W_{\text{loss}}}{W_0} = \frac{2kE^- a^{-2}}{\pi(E^+ a^{+2} + E^- a^{-2})} \int_0^y \sin^2(kx) dx = \frac{kE^- a^{-2}}{\pi(E^+ a^{+2} + E^- a^{-2})} \left(y - \frac{\sin(2ky)}{2k} \right), \quad (14)$$

where y should be substituted from (13). In Figure 13(c) we show the evolution of the signal shape for $a^-/a^+ = 1.5$, the change in α -discontinuity speed as well as the remnant non-zero signal of the compressive component can be easily observed. In Figure 13(d) the evolution of the energy obtained using the geometrical model is plotted for different amplitudes $a^-/a^+ = \{1.2, 1.5, 2\}$. Naturally, the larger the amplitude difference, the more energy remains in the signal. In the same figure, the remaining energy is estimated using (14) for the same amplitude ratios and it is shown with horizontal lines, the match between the model and the equation is perfect. Note that qualitatively the shape of transmission factor obtained for this simple signal is very similar to those observed for a random self-affine signal shown in Figure 9. Of course, the geometrical model cannot capture the full complexity of energy cascades and viscous damping, but it permits to understand better and predict rather accurately the change in the signal after it passes through a bimodular section.

10. Conclusions

A new concept for architected materials was developed in which the elastic asymmetry can be finely adjusted by combining internal contacts and components of different stiffness. Propagation of one-dimensional elastic waves in the resulting elastically asymmetric media was studied. The overlap of tensile and compressive wave components propagating at different speeds results in emergence of energy cascades leading to a partial or, in particular cases, almost complete annihilation of tensile and compressive wave components. This phenomenon was already known to the community but we investigated it from a new perspective, carried out a rather complete spectral analysis and considered a novel configuration with two segments of inverse asymmetry, which results in extreme damping of the incident signal. The efficient wave damping happens if the bimodular segment is chosen longer than the wave-overlap distance, Equation (4). The ratio of the overlap length to the incident wavelength scales as $L_o/\lambda_0 \sim 1/(\sqrt{\gamma}-1)$. The key advantage of the proposed architected materials consists in fact that the elastic asymmetry γ can be adjusted to be very high, which would enable to keep the damping device relatively small compared to the incident wavelength.

In the more realistic situation of an incident wave containing many modes, only partial annihilation can occur, however, the signal after passing through a relatively long bimodular segment appears “polarized” either to positive or negative deformation. This original observation was made in the study of self-affine incident wave packets (Gaussian envelope) passing through a bimodular section. This analysis permitted us to obtain a rather universal form of the ratio of transmitted to injected energy (transmission factor) with respect to the length of bimodular segment and also to obtain relevant normalizations. In addition, a simple model of geometrical overlap was developed and some simple analytical results for the transmission factor were obtained.

The demonstrated efficient damping and sign-polarization mechanisms can be used in shock absorbing and wave filtering systems, and, hypothetically, in seismic protection from surface waves. For further investigation, the one-dimensional model should be extended to two- and three-dimensional cases, where the compressive/tensile elastic asymmetry should be enhanced with shear asymmetry and complemented by elastic anisotropy.

The computational code for simulation of the one-dimensional wave propagation in asymmetric medium with absorbing boundaries is available in Supplementary material [65] as well as the data of hundreds of simulations and the scripts for their post-processing and figure plotting.

Conflicts of interest

The author declares no competing financial interest.

Acknowledgements

The author is grateful to Lev Truskinovsky for valuable discussions, to Samuel Forest for his encouragement, and to Arsen Subashiev for helpful remarks to the text.

Supplementary data

Supplementary material for this article (documented computational code, simulation data, scripts for the geometrical model and scripts for Figures 7, 8, 9, 10, 11, 13) is accessible at <https://doi.org/10.5281/zenodo.4461652>.

References

- [1] R. M. Jones, “Stress–strain relations for materials with different moduli in tension and compression”, *AIAA J.* **15** (1977), no. 1, p. 16-23.
- [2] C. Mauge, M. Kachanov, “Effective elastic properties of an anisotropic material with arbitrarily oriented interacting cracks”, *J. Mech. Phys. Solids* **42** (1994), no. 4, p. 561-584.
- [3] S. P. Lake, M. F. Hadi, V. K. Lai, V. H. Barocas, “Mechanics of a fiber network within a non-fibrillar matrix: model and comparison with collagen–agarose co-gels”, *Ann. Biomed. Eng.* **40** (2012), no. 10, p. 2111-2121.
- [4] A. Abhilash, B. M. Baker, B. Trappmann, C. S. Chen, V. B. Shenoy, “Remodeling of fibrous extracellular matrices by contractile cells: predictions from discrete fiber network simulations”, *Biophys. J.* **107** (2014), no. 8, p. 1829-1840.
- [5] J. Dirrenberger, S. Forest, D. Jeulin, “Towards gigantic RVE sizes for 3D stochastic fibrous networks”, *Int. J. Solids Struct.* **51** (2014), no. 2, p. 359-376.
- [6] N. Wang, K. Naruse, D. Stamenović, J. J. Fredberg, S. M. Mijailovich, I. M. Tolić-Nørrelykke, T. Polte, R. Mannix, D. E. Ingber, “Mechanical behavior in living cells consistent with the tensegrity model”, *Proc. Natl. Acad. Sci. USA* **98** (2001), no. 14, p. 7765-7770.
- [7] P. A. Janmey, M. E. McCormick, S. Rammensee, J. L. Leight, P. C. Georges, F. C. MacKintosh, “Negative normal stress in semiflexible biopolymer gels”, *Nat. Mater.* **6** (2007), no. 1, p. 48-51.
- [8] J. Notbohm, A. Lesman, P. Rosakis, D. A. Tirrell, G. Ravichandran, “Microbuckling of fibrin provides a mechanism for cell mechanosensing”, *J. R. Soc. Interface* **12** (2015), no. 108, article no. 20150320.
- [9] P. Ronceray, C. P. Broedersz, M. Lenz, “Fiber networks amplify active stress”, *Proc. Natl. Acad. Sci. USA* **113** (2016), no. 11, p. 2827-2832.
- [10] Z. Du, Y. Zhang, W. Zhang, X. Guo, “A new computational framework for materials with different mechanical responses in tension and compression and its applications”, *Int. J. Solids Struct.* **100** (2016), p. 54-73.
- [11] N. Boechler, G. Theocharis, S. Job, P. G. Kevrekidis, M. A. Porter, C. Daraio, “Discrete breathers in one-dimensional diatomic granular crystals”, *Phys. Rev. Lett.* **104** (2010), no. 24, article no. 244302.
- [12] K. Jayaprakash, Y. Starosvetsky, A. F. Vakakis, M. Peeters, G. Kerschen, “Nonlinear normal modes and band zones in granular chains with no pre-compression”, *Nonlinear Dyn.* **63** (2011), no. 3, p. 359-385.
- [13] A. Leonard, C. Chong, P. G. Kevrekidis, C. Daraio, “Traveling waves in 2D hexagonal granular crystal lattices”, *Granul. Matter* **16** (2014), no. 4, p. 531-542.

- [14] C. Guillemer, M. Clavel, G. Cailletaud, "Cyclic behavior of extruded magnesium: experimental, microstructural and numerical approach", *Int. J. Plast.* **27** (2011), no. 12, p. 2068-2084.
- [15] D. H. Warner, J. F. Molinari, "Deformation by grain boundary hinge-like behavior", *Mater. Lett.* **62** (2008), no. 1, p. 57-60.
- [16] B. Dean, B. Bhushan, "Shark-skin surfaces for fluid-drag reduction in turbulent flow: a review", *Philos. Trans. R. Soc. Lond. A* **368** (2010), no. 1929, p. 4775-4806.
- [17] A. Rafsanjani, Y. Zhang, B. Liu, S. M. Rubinstein, K. Bertoldi, "Kirigami skins make a simple soft actuator crawl", *Sci. Robot.* **3** (2018), no. 15, article no. eaar7555.
- [18] A. Rafsanjani, K. Bertoldi, "Buckling-induced kirigami", *Phys. Rev. Lett.* **118** (2017), no. 8, article no. 084301.
- [19] R. Desmorat, F. Gatuingt, F. Ragueneau, "Nonlocal anisotropic damage model and related computational aspects for quasi-brittle materials", *Eng. Fract. Mech.* **74** (2007), no. 10, p. 1539-1560.
- [20] R. Desmorat, S. Cantournet, "Modeling microdefects closure effect with isotropic/anisotropic damage", *Int. J. Damage Mech.* **17** (2008), no. 1, p. 65-96.
- [21] S. A. Ambartsumyan, A. A. Khachatryan, "Basic equations in the theory of elasticity for materials with different stiffness in tension and compression", *Mech. Solids* **1** (1966), no. 2, p. 29-34.
- [22] F. Tabaddor, "Two-dimensional bi-linear orthotropic elastic materials", *J. Compos. Mater.* **3** (1969), no. 4, p. 725-727.
- [23] F. Tabaddor, "Constitutive equations for bimodulus elastic materials", *AIAA J.* **10** (1972), no. 4, p. 516-518.
- [24] S. A. Ambartsumyan, "Equations of the plane problem heteroresisting or heteromodular theory of elasticity", *Izv. Akad. Nauk Armyanskoy SSR, Mekh.* **19** (1966), no. 2, p. 3-19.
- [25] S. A. Ambartsumyan, *Theory of Heteromodular Elasticity*, Nauka, Moscow, Russia, 1982.
- [26] D. Spence, J. Mkrтчian, "The Boussinesq problem for a material with different moduli in tension and compression", *Q. J. Mech. Appl. Math.* **30** (1977), no. 4, p. 449-466.
- [27] E. Lomakin, I. Rabotnov, "A theory of elasticity for an isotropic body with different moduli in tension and compression", *Mech. Solids* **13** (1978), no. 6, p. 25-30, in Russian, *Mekhanika Tverdogo Tela* **6** (1978), p. 29-34.
- [28] L. Baev, "Propagation of longitudinal and transverse waves in a multimodulus elastic medium", *J. Appl. Mech. Tech. Phys.* **50** (2009), no. 4, p. 691-697.
- [29] V. Ragozina, O. Dudko, "Propagation of converging spherical deformation waves in a heteromodular elastic medium", *J. Appl. Mech. Tech. Phys.* **57** (2016), no. 4, p. 701-708.
- [30] A. Green, J. Mkrтчian, "Elastic solids with different moduli in tension and compression", *J. Elast.* **7** (1977), no. 4, p. 369-386.
- [31] A. Curnier, Q.-C. He, P. Zysset, "Conewise linear elastic materials", *J. Elast.* **37** (1994), no. 1, p. 1-38.
- [32] J.-Y. Sun, H.-Q. Zhu, S.-H. Qin, D.-L. Yang, X.-T. He, "A review on the research of mechanical problems with different moduli in tension and compression", *J. Mech. Sci. Technol.* **24** (2010), no. 9, p. 1845-1854.
- [33] S. Nemat-Nasser, M. Hori, *Micromechanics: Overall Properties of Heterogeneous Materials*, vol. 37, Elsevier, Amsterdam, The Netherlands, 2013.
- [34] V. P. Maslov, P. P. Mosolov, "General theory of the solutions of the equations of motion of an elastic medium of different moduli", *J. Appl. Math. Mech.* **49** (1985), no. 3, p. 322-336.
- [35] S. Lepri, G. Casati, "Asymmetric wave propagation in nonlinear systems", *Phys. Rev. Lett.* **106** (2011), article no. 164101.
- [36] S. N. Gavrilov, G. C. Herman, "Wave propagation in a semi-infinite heteromodular elastic bar subjected to a harmonic loading", *J. Sound Vib.* **331** (2012), no. 20, p. 4464-4480.
- [37] A. V. Radostin, V. E. Nazarov, S. B. Kiyashko, "Propagation of nonlinear acoustic waves in bimodular media with linear dissipation", *Wave Motion* **50** (2013), no. 2, p. 191-196.
- [38] V. E. Nazarov, S. B. Kiyashko, A. V. Radostin, "Stationary waves in a bimodular rod of finite radius", *Wave Motion* **75** (2017), p. 72-76.
- [39] O. V. Dudko, A. A. Lapteva, K. Semenov, "About distribution of flat one-dimensional waves and their interaction with barrier in the media differently reacting to a stretching and compression", *Dal'nevostochnyi Matematicheskii Zh.* **6** (2005), no. 1, p. 94-105, in Russian.
- [40] M. S. Kuznetsova, E. Pasternak, A. V. Dyskin, "Analysis of wave propagation in a discrete chain of bilinear oscillators", *Nonlinear Process. Geophys.* **24** (2017), no. 3, p. 455-460.
- [41] Z. Lu, A. N. Norris, "Non-reciprocal wave transmission in a bilinear spring-mass system", *J. Vibr. Acoust.* **142** (2020), no. 2, article no. 021006.
- [42] L. Fang, A. Darabi, A. Mojahed, A. F. Vakakis, M. J. Leamy, "Broadband non-reciprocity with robust signal integrity in a triangle-shaped nonlinear 1D metamaterial", *Nonlinear Dyn.* **100** (2020), p. 1-13.
- [43] B. Liang, B. Yuan, J.-c. Cheng, "Acoustic diode: rectification of acoustic energy flux in one-dimensional systems", *Phys. Rev. Lett.* **103** (2009), no. 10, article no. 104301.
- [44] Z. Lu, A. N. Norris, "Unilateral and nonreciprocal transmission through bilinear spring systems", *Extreme Mech. Lett.* **42** (2021), article no. 101087.

- [45] Y. Benveniste, "One-dimensional wave propagation in materials with different moduli in tension and compression", *Int. J. Eng. Sci.* **18** (1980), no. 6, p. 815-827.
- [46] D. Kharenko, C. Padovani, A. Pagni, G. Pasquinelli, L. Semin, "Free longitudinal vibrations of bimodular beams: a comparative study", *Int. J. Struct. Stab. Dyn.* **11** (2011), no. 01, p. 23-56.
- [47] P.D. Lax, *Hyperbolic Systems of Conservation Laws and the Mathematical Theory of Shock Waves*, SIAM, Philadelphia, PA, USA, 1973.
- [48] A. Kulikovskii, L. Pekurovskaya, "On fronts of strong and weak discontinuities in solutions of the equations of different-modulus elasticity theory", *J. Appl. Math. Mech.* **53** (1989), no. 2, p. 230-235.
- [49] A. Kulikovskii, L. Pekurovskaya, "Longitudinal waves in an elastic medium with a piecewise-linear dependence of the stress on the strain", *J. Appl. Math. Mech.* **54** (1990), no. 5, p. 663-668.
- [50] R. Abeyaratne, J. K. Knowles, "Wave propagation in linear, bilinear and trilinear elastic bars", *Wave Motion* **15** (1992), no. 1, p. 77-92.
- [51] M. Lucchesi, A. Pagni, "Longitudinal oscillations of bimodular rods", *Int. J. Struct. Stab. Dyn.* **5** (2005), no. 01, p. 37-54.
- [52] L. Zuo, A. Curnier, "Non-linear real and complex modes of conewise linear systems", *J. Sound Vib.* **174** (1994), no. 3, p. 289-313.
- [53] J. M. T. Thompson, R. Ghaffari, "Chaos after period-doubling bifurcations in the resonance of an impact oscillator", *Phys. Lett. A* **91** (1982), no. 1, p. 5-8.
- [54] S. Natsiavas, "Dynamics of multiple-degree-of-freedom oscillators with colliding components", *J. Sound Vib.* **165** (1993), no. 3, p. 439-453.
- [55] R. V. Goldstein, S. V. Kuznetsov, M. A. Khudyakov, "Study of forced vibrations of the Kelvin-Voigt model with an asymmetric spring", *Mech. Solids* **50** (2015), no. 3, p. 294-304.
- [56] J. Awrejcewicz, C.-H. Lamarque, *Bifurcation and Chaos in Nonsmooth Mechanical Systems*, vol. 45, World Scientific, Singapore, 2003.
- [57] D. M. Kochmann, W. J. Drugan, "Dynamic stability analysis of an elastic composite material having a negative-stiffness phase", *J. Mech. Phys. Solids* **57** (2009), no. 7, p. 1122-1138.
- [58] P. Wang, F. Casadei, S. Shan, J. C. Weaver, K. Bertoldi, "Harnessing buckling to design tunable locally resonant acoustic metamaterials", *Phys. Rev. Lett.* **113** (2014), no. 1, article no. 014301.
- [59] B. Florijn, C. Coulais, M. van Hecke, "Programmable mechanical metamaterials", *Phys. Rev. Lett.* **113** (2014), no. 17, article no. 175503.
- [60] O. Lourie, D. M. Cox, H. D. Wagner, "Buckling and collapse of embedded carbon nanotubes", *Phys. Rev. Lett.* **81** (1998), no. 8, p. 1638-1641.
- [61] A. Sears, R. C. Batra, "Macroscopic properties of carbon nanotubes from molecular-mechanics simulations", *Phys. Rev. B* **69** (2004), no. 23, article no. 235406.
- [62] L. R. Meza, S. Das, J. R. Greer, "Strong, lightweight, and recoverable three-dimensional ceramic nanolattices", *Science* **345** (2014), no. 6202, p. 1322-1326.
- [63] V. Tournat, V. E. Gusev, "Nonlinear effects for coda-type elastic waves in stressed granular media", *Phys. Rev. E* **80** (2009), no. 1, article no. 011306.
- [64] A. C. Eringen, *Mechanics of Continua*, Robert E. Krieger Publishing Co., Huntington, NY, USA, 1980.
- [65] V. A. Yastrebov, "Code, data and scripts to study wave dynamics in asymmetric material", 2021, Zenodo, <https://doi.org/10.5281/zenodo.4461652>.